

# In-Situ Hydrogenation Strategies on Vanadium Oxide Hole-Selective Contact for Efficiency Crystalline Silicon Solar Cells

Anzhi Xie, Qingxian Nong, Kaiming Shang, Yiwei Sun, Jian He,\* and Pingqi Gao\*

Surface passivation and contact resistance are two main parameters to optimize the photoelectric performance of crystalline silicon/transition metal oxides (c-Si/TMO) heterojunction solar cells. However, most studies focus on the introduction of dielectric layers at the heterojunction interface to improve the passivating contact performance, with limited attention given to optimizing the TMO film for improved photoelectric performance. Herein, an in-situ hydrogen plasma treatment (HPT) process is employed to modulate the photoelectric properties of vanadium oxide ( $V_2O_x$ ) film as well as the c-Si/ $V_2O_x$  interface. With increased O vacancy density in  $V_2O_x$  film and increased H bonds at c-Si/ $V_2O_x$  interface, this c-Si/HPT- $V_2O_x$  contact shows reduced contact resistivity and improved passivation properties. A satisfied power conversion efficiency (PCE) of close to 23% is achieved on *p*-type c-Si solar cells with full area HPT- $V_2O_x$  rear hole selective contacts. The results show the high potential of  $V_2O_x$  as thermal and environmental stable hole selective contact for photovoltaic applications.

## 1. Introduction

Crystalline silicon (c-Si) solar cells still dominate the photovoltaic (PV) market due to their high potential for green electricity production. Currently, the mainstream c-Si technology is gradually shifting from passivated emitter and rear contact to passivating contact technology, such as tunnel oxide passivating contact

(TOPCon) and c-Si heterojunction (SHJ) solar cells.<sup>[1]</sup> The implementation of passivating contact technology effectively reduces interface carrier recombination, thereby significantly increasing the open circuit voltage ( $V_{OC}$ ) and enhancing the power conversion efficiency (PCE) of the solar cells.<sup>[2]</sup> However, the necessity of using intrinsic or highly doped Si films as passivating and carrier selective transporting layers in both TOPCon and SHJ solar cells pose several challenges. These include optical parasitic absorption and free carrier absorption losses, which can limit the short-circuit current density ( $J_{SC}$ ) of the solar cells.<sup>[3]</sup>

To achieve a higher  $J_{SC}$  and further improve the PCE of c-Si solar cells, significant efforts have been made to replace doped Si layers with functional metal oxides.<sup>[4]</sup> Generally, low work functional fluorides with wide bandgap, such as

lithium fluoride,<sup>[5,6]</sup> europium fluoride,<sup>[7]</sup> aluminum fluoride,<sup>[8]</sup> and strontium fluoride<sup>[9]</sup> have been widely exploited as electron-selective transporting layers (ETLs). Additionally, metal oxides, such as titanium oxide,<sup>[10–12]</sup> zinc oxide,<sup>[13–15]</sup> and magnesium oxide,<sup>[16–18]</sup> which exhibit negligible conduction band offset with c-Si, are also suitable for electron-selective transport. In contrast to ETLs, which offer a variety of material choices and modifications, ideal hole-selective transporting layers (HTLs) must exhibit a high work function (WF), low hole transporting resistance, and high optical transmittance. At present, molybdenum oxide ( $MoO_x$ )<sup>[19–25]</sup> and vanadium oxide ( $V_2O_x$ )<sup>[26–32]</sup> are the most promising materials for hole-selective contacts in c-Si solar cells.

In the development of HTLs, the passivation and contact properties of c-Si/HTL contacts are typically enhanced by introducing dielectric layers at each contact interface. E.g., Geissbuhler et al. obtained a PCE of 22.5% by inserting a thin intrinsic hydrogenated amorphous silicon (a-Si:H) passivating layer between c-Si and  $MoO_x$ , which improved the interface passivation performance.<sup>[19]</sup> Cao et al. further optimized this approach by treating the intrinsic a-Si:H layer with boron radicals plasma before  $MoO_x$  deposition, effectively controlling the oxygen vacancies and achieving a PCE of 23.83%.<sup>[21]</sup> Besides intrinsic a-Si:H, other oxide dielectric layers, such as silicon oxides ( $SiO_x$ )<sup>[8,33]</sup> and aluminium oxide,<sup>[34,35]</sup> are also frequently employed as interface passivating layer to enhance the passivating contact

A. Xie, Q. Nong, K. Shang, Y. Sun, J. He, P. Gao  
School of Materials  
Shenzhen Campus of Sun Yat-sen University  
No. 66, Gongchang Road, Shenzhen, Guangdong 518107, P. R. China  
E-mail: [hejian7@mail.sysu.edu.cn](mailto:hejian7@mail.sysu.edu.cn); [gaopq3@mail.sysu.edu.cn](mailto:gaopq3@mail.sysu.edu.cn)

J. He, P. Gao  
Institute for Solar Energy Systems  
Guangdong Engineering Technology Research Center for Sustainable Photovoltaic Technology and Equipment  
State Key Laboratory of Optoelectronic Materials and Technologies  
Sun Yat-sen University  
Guangzhou 510275, P. R. China  
J. He, P. Gao  
Jiangsu Collaborative Innovation Center of Photovoltaic Science and Engineering  
Changzhou University  
Changzhou 213164, China

The ORCID identification number(s) for the author(s) of this article can be found under <https://doi.org/10.1002/sml.202410492>

DOI: 10.1002/sml.202410492

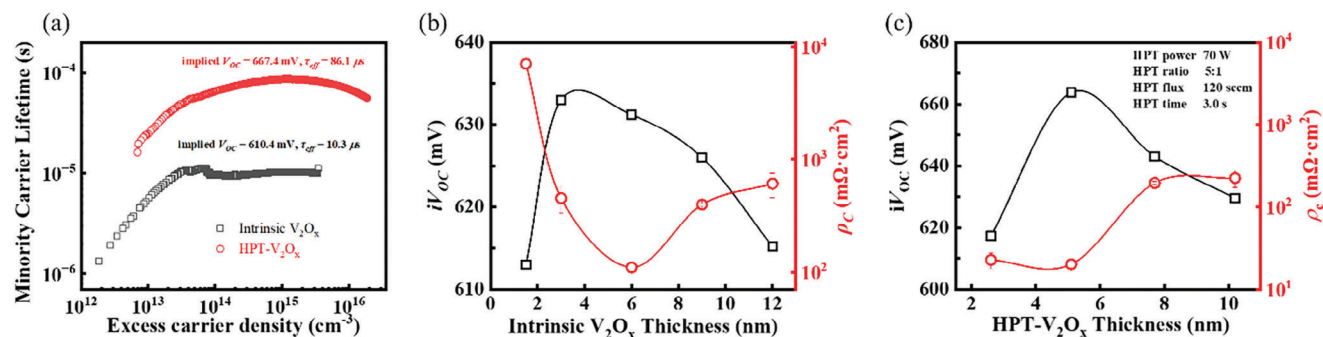


**Figure 1.** Passivation and contact properties of Intrinsic and HPT-V<sub>2</sub>O<sub>x</sub>. a) Effective minority carrier lifetime of *p*-Si wafers with symmetrical intrinsic and HPT-V<sub>2</sub>O<sub>x</sub> contact. V<sub>2</sub>O<sub>x</sub> thickness dependent  $iV_{OC}$  and contact resistivity of b) intrinsic-V<sub>2</sub>O<sub>x</sub> and c) HPT-V<sub>2</sub>O<sub>x</sub>.

performance of c-Si/HTL contacts. Li et al. introduced an ultra-thin SiO<sub>x</sub> tunnel layer via ultraviolet ozone pretreatment to suppress the redox reaction at c-Si/V<sub>2</sub>O<sub>x</sub> interface, resulting in a PCE of 21.01%.<sup>[30]</sup> This PCE was further improved to 22.03% by inserting a SiO<sub>x</sub>/NiO<sub>x</sub> stack between V<sub>2</sub>O<sub>x</sub>/Ag interface to improve the hole selectivity.<sup>[31]</sup>

Compared to regulating the passivation performance of c-Si/HTL contacts through the introduction of interfacial dielectric layers, there are fewer reports on improving the passivation contact performance by tuning the optoelectronic properties of HTLs. This is primarily due to the lack of advanced deposition technologies for HTL materials. Typically, MoO<sub>x</sub> or V<sub>2</sub>O<sub>x</sub> HTLs are deposited via thermal evaporation using molybdenum trioxide or V<sub>2</sub>O<sub>5</sub> powder, making it challenging to control their elemental composition and structure during the deposition process. Most recently, Zhang et al. demonstrated that MoO<sub>x</sub> thin films with low oxygen concentration deposited by thermal evaporation of molybdenum dioxide powder, exhibit improved photoelectric properties.<sup>[25]</sup> However, fine-tuning the optoelectronic properties of HTL thin films through the deposition process remains challenging. Therefore, from the perspective of material sustainability, developing advanced thin film deposition techniques and deliberately regulating the photoelectric properties of HTL thin films are of great significance for the continuous improvement of c-Si solar cells.

V<sub>2</sub>O<sub>x</sub> has been reported to exhibit a higher WF<sup>[36]</sup> and superior surface passivation properties compared to MoO<sub>x</sub>.<sup>[37]</sup> However, the maximum PCE achieved with an a-Si:H/V<sub>2</sub>O<sub>x</sub> rear contact configuration is 22.8%,<sup>[32]</sup> which remains significantly lower than the 23.83% PCE reported for devices employing an a-Si:H/MoO<sub>x</sub> front contact.<sup>[21]</sup> In this study, a thin-film V<sub>2</sub>O<sub>x</sub> HTL was deposited using an atomic layer deposition (ALD) process, combined with an in-situ hydrogen plasma treatment (HPT) process to modulate the photoelectric properties of V<sub>2</sub>O<sub>x</sub> film. By rationally controlling the HPT process, the O vacancy concentration in the V<sub>2</sub>O<sub>x</sub> film as well as the H and C content at the c-Si/V<sub>2</sub>O<sub>x</sub> interface can be effectively regulated. This dual regulation improves both the passivation and contact performance of the c-Si/V<sub>2</sub>O<sub>x</sub> hole-selective contact. Eventually, environmental and thermally stable *p*-type c-Si solar cells with satisfied PCE of close to 23% were achieved by solely using full area V<sub>2</sub>O<sub>x</sub> as rear hole-selective contacts.

## 2. Result and Discussion

### 2.1. Passivation and Contact Properties of c-Si/V<sub>2</sub>O<sub>x</sub> Contact

Intrinsic V<sub>2</sub>O<sub>x</sub> films are deposited by using ALD process, with Vanadium (V) tri-*i*-propoxy oxide serving as the V precursor and deionized water (DI H<sub>2</sub>O) as the O precursor. For the HPT-V<sub>2</sub>O<sub>x</sub> films, hydrogen plasma is continuously introduced during the deposition of V<sub>2</sub>O<sub>x</sub> films, as illustrated in Figure S1 (Supporting Information), including *n* cycle of intrinsic V<sub>2</sub>O<sub>x</sub> plus one cycle HPT. The hydrogenation within the V<sub>2</sub>O<sub>x</sub> films can be controlled by optimizing the HPT process. Figure 1a shows the passivation properties of *p*-type silicon (*p*-Si) wafers symmetrically coated with intrinsic and HPT-V<sub>2</sub>O<sub>x</sub> films, characterized using transient photoconductance decay method. When intrinsic V<sub>2</sub>O<sub>x</sub> films ( $\approx$ 6 nm) are symmetrically deposited on both sides of the *p*-Si wafers, they exhibit a very low effective minority carrier lifetime ( $\tau_{eff}$ ) of only 10  $\mu$ s and an implied  $V_{OC}$  ( $iV_{OC}$ ) of 610 mV. In contrast, the samples coated with thin HPT-V<sub>2</sub>O<sub>x</sub> films show significantly improved surface passivation, with a relatively high  $\tau_{eff}$  of 86  $\mu$ s and an  $iV_{OC}$  of 667 mV. This indicates that the in-situ HPT process can effectively enhance passivation properties even without additional passivating interlayers.

The thickness dependent passivation and contact properties of the *p*-Si/V<sub>2</sub>O<sub>x</sub> contact using intrinsic and HPT-V<sub>2</sub>O<sub>x</sub> films are presented in Figures 1b,c, respectively. For both intrinsic and HPT-V<sub>2</sub>O<sub>x</sub> contacts, the optimal passivation and contact performance are achieved at a V<sub>2</sub>O<sub>x</sub> thickness of  $\approx$ 6 nm. Specifically, the *p*-Si/intrinsic-V<sub>2</sub>O<sub>x</sub> contact exhibits an  $iV_{OC}$  of  $\approx$ 610 mV and a contact resistivity ( $\rho_c$ ) of  $\approx$ 60 m $\Omega$  cm<sup>2</sup>, while the *p*-Si/HPT-V<sub>2</sub>O<sub>x</sub> contact shows an  $iV_{OC}$  of  $\approx$ 660 mV and a  $\rho_c$  of  $\approx$ 20 m $\Omega$  cm<sup>2</sup>. Further increasing the V<sub>2</sub>O<sub>x</sub> thickness significantly deteriorates both passivation and contact properties, primarily due to the intensified tensile stress in the V<sub>2</sub>O<sub>x</sub> film during deposition.<sup>[38]</sup> Additionally, the degradation of contact properties is also attributed to the increased bulk resistance of the V<sub>2</sub>O<sub>x</sub> films.<sup>[39]</sup> Notably, at the same thickness, the passivation and contact properties using HPT-V<sub>2</sub>O<sub>x</sub> films are significantly better than those of intrinsic-V<sub>2</sub>O<sub>x</sub> films.

To further optimize the HPT process during the V<sub>2</sub>O<sub>x</sub> film deposition, we systematically varied the parameters such as the HPT ratio (defined as the V precursor to H plasma pulse cycle ratio) and HPT pulse time. Figure 2a illustrates the passivation

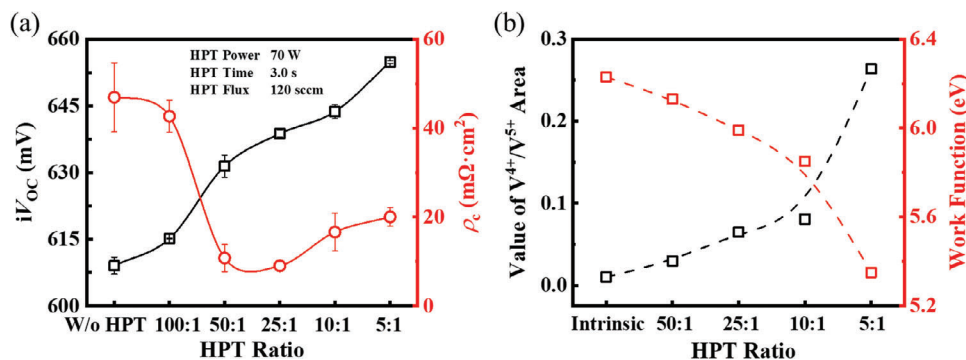


**Figure 2.** Passivation and contact properties of HPT- $V_2O_x$  at different HPT ratio. a) HPT ratio dependent passivation and contact properties of  $p$ -Si/ $V_2O_x$  contacts. b) The value of  $V^{4+}/V^{5+}$  area fitting from V 2p XPS and the WF of  $V_2O_x$  films as a function of HPT ratio.

and contact properties of  $p$ -Si/ $V_2O_x$  contacts subjected to different HPT ratios, ranging from 100:1 to 5:1, while maintaining the same film thickness. Compared to intrinsic  $p$ -Si/ $V_2O_x$  contacts, the introduction of HPT process will significantly enhance passivation properties and reduce the contact resistivity. Additionally, the dependence of passivation and contact performance on HPT pulse time for  $p$ -Si/ $V_2O_x$  contacts is also investigated in Figure S2 (Supporting Information). The passivation performance will continuously improve with increasing H plasma pulse time. However, the optimal contact resistivity is achieved with H plasma pulse time of 3 s.

X-ray photoelectron spectroscopy (XPS) analysis was used to investigate the chemical bonding of  $V_2O_x$  films with and without HPT process, as depicted in Figure S3 (Supporting Information). For all  $V_2O_x$  films, both with and without HPT,  $V^{4+}$  and  $V^{5+}$  components were observed in the V 2p core level, with the  $V^{4+}$  and  $V^{5+}$  peaks centered at 516.9 eV and 516.0 eV, respectively.<sup>[40,41]</sup> For the intrinsic  $V_2O_x$  films, the O/V ratio was determined to be 2.66 (Figure S3a,f, Supporting Information), and the  $V^{4+}/V^{5+}$  ratio was calculated as 0.01 (Figure 2b), indicating that  $V^{5+}$  is the predominant species in these intrinsic  $V_2O_x$  films. In contrast, for the  $V_2O_x$  films subjected to the HPT process, such as an HPT ratio of 5:1, the O/V ratio was reduced to 2.46 (Figure S3e,f, Supporting Information), and the  $V^{4+}/V^{5+}$  ratio was increased to  $\approx 0.26$  (Figure 2b). The O/V ratios and  $V^{4+}/V^{5+}$  ratios of  $V_2O_x$  films with different HPT process ratios ranging from 50:1 to 5:1 were summarized in Figure S3f (Supporting Information) and Figure 2b, with the corresponding WFs of each film marked in Figure 2b. As the HPT process cycle ratio increased during  $V_2O_x$  film deposition, a higher concentration of  $V^{4+}$  components together with a higher O vacancy concentration can be observed in the  $V_2O_x$  films, resulting in decreased WF values. This increased concentration of  $V^{4+}$  components is likely responsible for the improved contact properties of the  $p$ -Si/HPT- $V_2O_x$  contact.<sup>[25]</sup>

## 2.2. Passivation and Transport Mechanism of c-Si/ $V_2O_x$ Contact

To investigate the effect of the in-situ HPT process during  $V_2O_x$  film deposition on the passivation improvement of  $p$ -Si/ $V_2O_x$  contacts, time-of-flight secondary ion mass spectrometry (ToF-SIMS) was used to analyze the  $p$ -Si/ $V_2O_x$  contacts with and without the HPT process. Figure 3a shows the distribution of H

throughout the  $p$ -Si/ $V_2O_x$  contact. Compared with intrinsic  $V_2O_x$  films, a higher H concentration was detected throughout the  $V_2O_x$  film and  $p$ -Si/ $V_2O_x$  interface when an additional HPT process was introduced during  $V_2O_x$  film deposition. This increased H concentration at the  $p$ -Si/ $V_2O_x$  interface can effectively passivate Si dangling bonds, thereby reducing carrier recombination. This enhancement in Si-H bonds is further evidenced by Fourier transform infrared spectroscopy (FTIR, 650–4000  $cm^{-1}$ ) measurements, as shown in Figure S4 (Supporting Information). In the FTIR spectrum, the strong absorption bands at  $\approx 1100$   $cm^{-1}$  and 970  $cm^{-1}$  correspond to the stretching vibrations of V–O ( $V^{4+}$ ) and V–O ( $V^{5+}$ ) bonds, indicating the presence of oxygen vacancies in the  $V_2O_x$  films.<sup>[42]</sup> The small absorption band at 1000–1200  $cm^{-1}$  is attributed to Si–O bonds of an ultra-thin  $SiO_x$  interlayer that forms spontaneously on the c-Si surface during the thermal ALD process. The large absorption band at 1700–2100  $cm^{-1}$  is assigned to the stretching mode of the Si–H bonds, showing a more pronounced absorption band for the HPT- $V_2O_x$  contact.<sup>[43]</sup> Since undesired carbon (C) on the Si surface will cause additional carrier recombination, the distribution of C concentration throughout the  $p$ -Si/ $V_2O_x$  contact is also presented in Figure 3b for both intrinsic- $V_2O_x$  and HPT- $V_2O_x$  contacts.<sup>[44]</sup> It shows that when introducing H plasma during  $V_2O_x$  film deposition, a reduced C concentration at the  $p$ -Si/ $SiO_x$ / $V_2O_x$  interface can be observed by forming C-H complexes.<sup>[45]</sup>

To validate the experimental analyses and further elucidate the passivating contact properties of the HPT- $V_2O_x$  contact, density functional theory (DFT) calculations were conducted to study the thermodynamic distribution of hydrogen in the c-Si/ $V_2O_x$  contact and its influence on charge balance. Extra hydrogen, considered as interstitial hydrogen ( $H_i$ ), was inserted into the c-Si/ $V_2O_x$  heterojunction supercell model under different chemical environments, including interface Si–H, interface O–H, and  $H_i$  in bulk  $V_2O_x$ . The optimized ball-and-stick structures of these configurations are shown in Figure S5 (Supporting Information). The formation energy of these  $H_i$  positions at the c-Si/ $V_2O_x$  heterojunction is summarized in Table S1 (Supporting Information). For the  $H_i$  position at the c-Si/ $V_2O_x$  interface, it tends to bond with Si atoms rather than O atoms due to the lower formation energy of Si–H (–1.09 eV) compared to O–H (–0.74 eV). This aligns with FTIR results, where the H in HPT- $V_2O_x$  films is observed to form Si–H bonds with minimal changes in –OH groups, as shown in Figure S4 (Supporting Information). For the

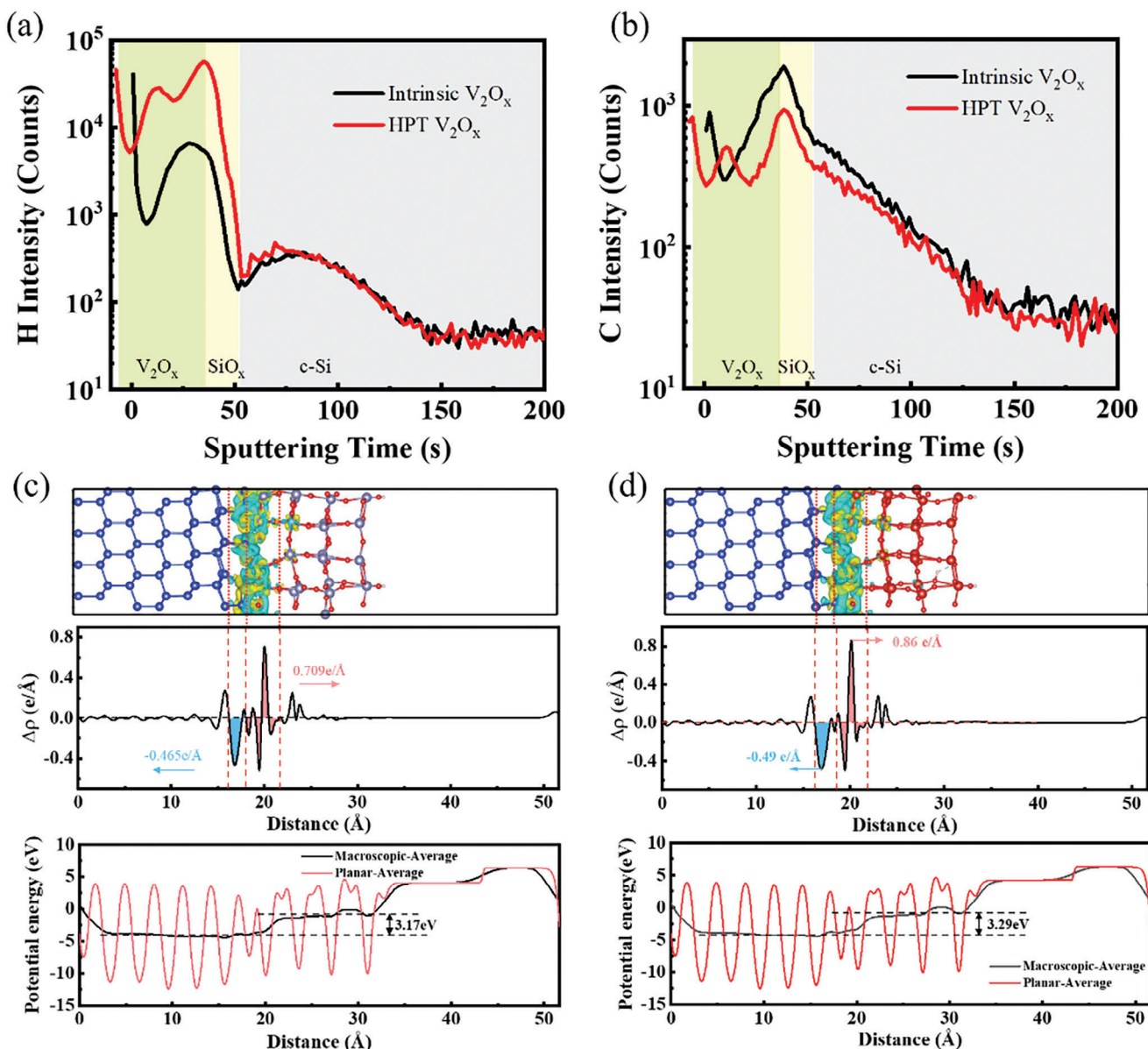


**Figure 3.** Passivation mechanism of c-Si/HPT-V<sub>2</sub>O<sub>x</sub> contact. The ToF-SIMS profiles of a) hydrogen and b) carbon intensity as a function of the sputter time for the c-Si/intrinsic-V<sub>2</sub>O<sub>x</sub> and c-Si/HPT-V<sub>2</sub>O<sub>x</sub> stack. The planar-averaged electron density difference  $\Delta\rho$ , the macroscopic average and planar average of potential energy for c) perfect c-Si/V<sub>2</sub>O<sub>x</sub> and d) c-Si/interface-H/HPT-V<sub>2</sub>O<sub>x</sub> configuration.

H<sub>i</sub> position in bulk V<sub>2</sub>O<sub>x</sub>, it tends to be doped in bulk V<sub>2</sub>O<sub>x</sub>, forming O–H bonds, corroborated by the XPS/UPS results in Figure 2b.

Furthermore, the planar-averaged electron density difference ( $\Delta\rho$ ), along with the macroscopic average and planar average of potential energy for the perfect c-Si/V<sub>2</sub>O<sub>x</sub> contact supercell and different H-incorporated supercells, are calculated as shown in Figure 3 and Figure S6 (Supporting Information). After introducing extra H at the c-Si/V<sub>2</sub>O<sub>x</sub> interface, the  $\Delta\rho$  on the c-Si side becomes more negative (shaded in blue), while the  $\Delta\rho$  on the V<sub>2</sub>O<sub>x</sub> side (shaded in red) becomes more positive, suggesting that electrons are partly transferred from c-Si to the V<sub>2</sub>O<sub>x</sub> side (compared Figure S6a, Supporting In-

formation to Figure 3c). Moreover, when incorporating interfacial H at the c-Si/V<sub>2</sub>O<sub>x</sub> contact, the macroscopic average potential energy difference of V<sub>2</sub>O<sub>x</sub> with respect to c-Si becomes much higher (3.17 eV to 3.36 eV), clearly indicating that the extra H incorporated at the c-Si/V<sub>2</sub>O<sub>x</sub> interface promotes more electron accumulation close to the c-Si interface. However, when considering extra H<sub>i</sub> in bulk V<sub>2</sub>O<sub>x</sub>, it causes negative effects, showing a lower macroscopic average potential energy difference of V<sub>2</sub>O<sub>x</sub> with respect to c-Si (3.08 eV to 3.17 eV, shown in Figure S6b, Supporting Information; Figure 3c). Therefore, when considering the introduction of H<sub>i</sub> into bulk V<sub>2</sub>O<sub>x</sub> along with H bonds at the c-Si/V<sub>2</sub>O<sub>x</sub> interface (shown in Figure 3d), the  $\Delta\rho$  decreases on the c-Si side and increases on the V<sub>2</sub>O<sub>x</sub> side overall. Additionally,



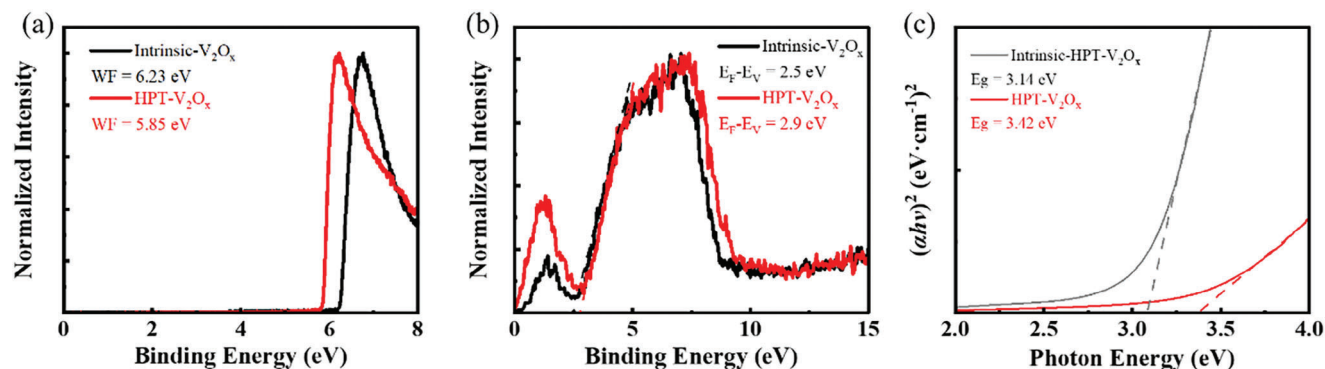


**Figure 4.** Photoelectrical properties of intrinsic- $V_2O_x$  and HPT- $V_2O_x$  film. a) The secondary electron cutoff spectrum and b) valence band spectrum of intrinsic- $V_2O_x$  and HPT- $V_2O_x$  films detected from UPS measurements. c) Tauc plot for intrinsic- $V_2O_x$  and HPT- $V_2O_x$  films.

the macroscopic average potential energy difference of HPT- $V_2O_x$  (3.29 eV) relative to c-Si is also higher than that of intrinsic  $V_2O_x$  (3.17 eV), indicating improved field-effect passivation.<sup>[35]</sup>

The electronic structure of  $V_2O_x$  films, with and without the HPT process, was investigated using ultraviolet photoelectron spectroscopy (UPS). Figure 4a shows the UPS secondary electron cutoff analysis of  $V_2O_x$  films with and without the HPT process after Argon ion sputtering. For the intrinsic  $V_2O_x$  film, a high WF value of 6.23 eV was detected. However, when the HPT process was introduced during  $V_2O_x$  film deposition, a lower WF of 5.85 eV was observed. This decrease in WF is mainly attributed to the increase in oxygen vacancies due to H incorporation. The valence band spectrum of  $V_2O_x$  films, with and without the HPT process, is also shown in Figure 4b, indicating that a higher valence band value from the Fermi energy level can be determined when hydrogen is doped into the  $V_2O_x$  film.

Figure 4c shows the Tauc optical bandgaps of the  $V_2O_x$  films with and without the HPT process, extracted from the transmittance curves in Figure S7 (Supporting Information). The bandgap increases from 3.14 eV for the intrinsic  $V_2O_x$  film to 3.42 eV for the HPT- $V_2O_x$  film. Combined with the optical and electrical characterization presented above, the calculated energy band diagrams of the  $p$ -Si/ $V_2O_x$  contact with intrinsic  $V_2O_x$  and HPT- $V_2O_x$  films as hole-selective contacts are illustrated in Figure S8 (Supporting Information). For the  $p$ -Si/intrinsic- $V_2O_x$  contact, the larger density of interfacial defects, the band offset between the conduction band position of intrinsic  $V_2O_x$  and the valence band position of  $p$ -Si, along with the relatively higher valence band energy of intrinsic  $V_2O_x$ , impede the effective transport of holes, resulting in poorer passivating contact performance. However, when hydrogen is introduced into the  $V_2O_x$  film and the  $p$ -Si/ $V_2O_x$  interface, the interfacial defects are effectively passivated, facilitating the collection of holes accumulated at the  $p$ -Si surface.<sup>[2]</sup>

### 2.3. PV Performance of c-Si Solar Cells Using $V_2O_x$ as Hole Selective Contact

To investigate the passivation and contact properties of the HPT- $V_2O_x$  film at the solar cell device level, we demonstrate proof-of-concept  $p$ -Si solar cells featuring a front-side heavily phosphorus-

diffused ( $n^+$ ) emitter and a rear-side full-area HPT- $V_2O_x$  contact, as shown in Figure 5a. The front-side emitter is coated with  $SiN_x$  passivation and anti-reflective layer, followed by screen-printed Ag grids. The rear-side metallization is achieved through thermally evaporated Ag full-area electrodes. A cross-sectional high-resolution transmission electron microscopy (HR-TEM) image of the  $p$ -Si/ $V_2O_x$ /Ag contact is also illustrated in Figure 5a, revealing an unexpected thin  $SiO_x$  interlayer  $\approx 1.0$  nm thick between the  $p$ -Si and  $V_2O_x$  film. The elemental distribution of the  $p$ -Si/ $V_2O_x$ /Ag contact is further analyzed using energy-dispersive X-ray spectroscopy (EDX) measurements, as depicted in Figure 5b, revealing distinct interfaces between each layer of the stack.

The current density-voltage curves of the  $p$ -Si solar cells with three configurations, without a  $V_2O_x$  contact layer, with an intrinsic  $V_2O_x$  rear contact, and with an HPT- $V_2O_x$  rear contact, are shown in Figure 5c and Figure S9 (Supporting Information). The corresponding PV parameters are summarized in Table S2 (Supporting Information). For the solar cells without using  $V_2O_x$ , the PCE is  $\approx 19.48\%$  with low  $V_{OC}$  of 0.634 V,  $J_{SC}$  of  $39.2 \text{ mA cm}^{-2}$ , and FF of 78.4%. The external quantum efficiency (EQE) and internal quantum efficiency (IQE) spectra within the long wavelength are relatively low with respect to the device with  $V_2O_x$  hole transport layers, attributed to the poor passivation at the rear surface. When using intrinsic- $V_2O_x$  as a full-area hole-selective contact, an enhanced PCE of 20.46% is achieved, with  $V_{OC}$  of 0.645 V,  $J_{SC}$  of  $40.4 \text{ mA cm}^{-2}$ , and FF of 78.5%. This PV performance is significantly improved when utilizing HPT- $V_2O_x$  as the hole-selective contact, featuring a best PCE of 22.93%,  $V_{OC}$  of 0.677 V,  $J_{SC}$  of  $41.4 \text{ mA cm}^{-2}$ , and FF of 81.8%. This enhanced PV performance for the HPT- $V_2O_x$  contacted device can be attributed to improved surface passivation and contact performance between  $p$ -Si and the Ag electrode, as discussed above. The  $J_{SC}$  values of both the intrinsic and HPT- $V_2O_x$  contacted solar cells are further calibrated by the EQE measurement, along with the integrated  $J_{SC}$  values, as shown in Figure 5d. A noticeable enhancement in the EQE values, especially in the long-wavelength range, is observed for the HPT- $V_2O_x$  contacted device, indicating reduced carrier recombination losses and improved hole-selective collection ability at the rear-side contact. As shown in Figure S10 (Supporting Information), a noticeable enhancement in the IQE values in the long-wavelength range is observed for the HPT- $V_2O_x$  compared to the intrinsic  $V_2O_x$ . This observation further confirms

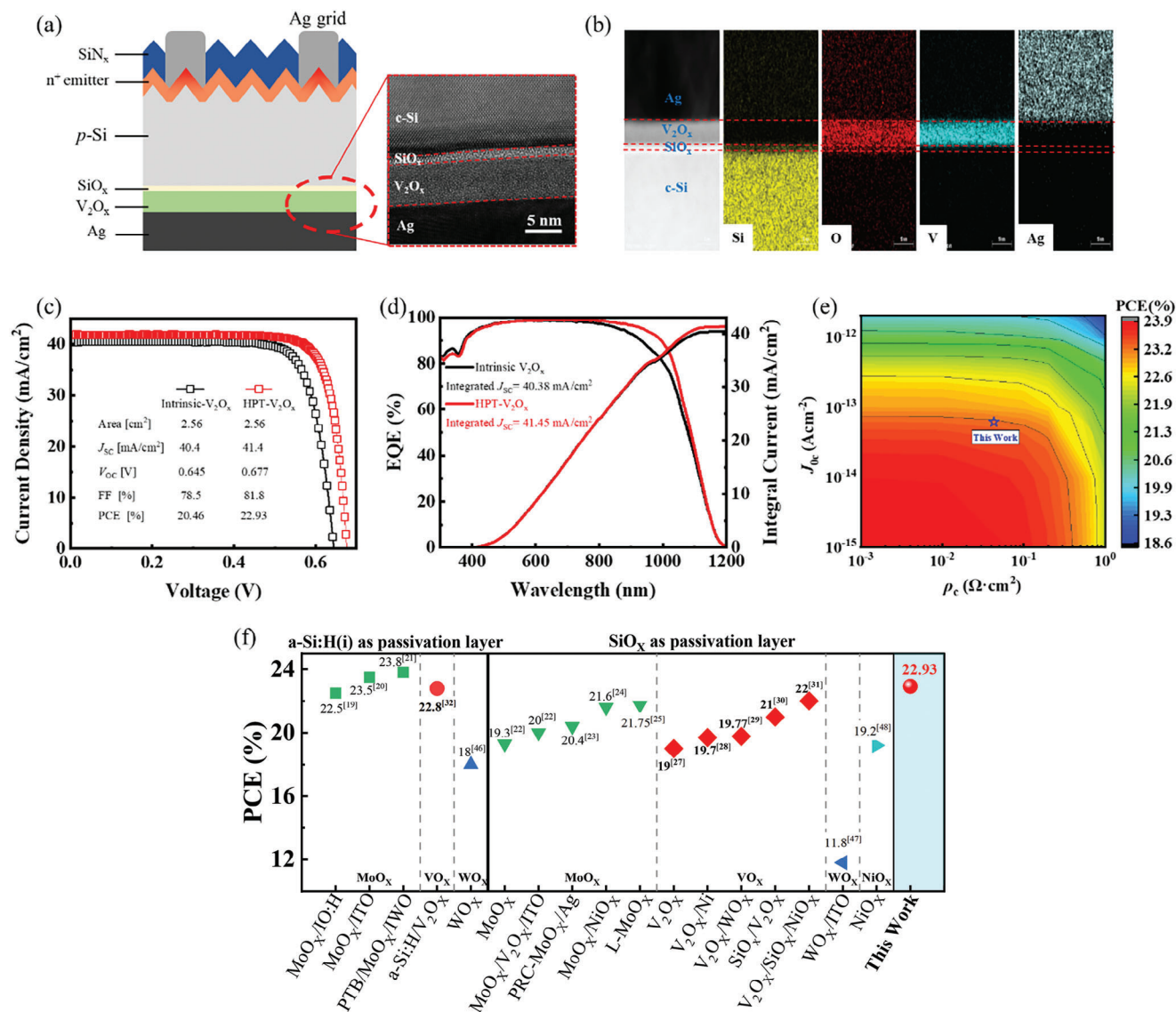


**Figure 5.** PV performance of *p*-Si solar cells based on V<sub>2</sub>O<sub>x</sub> hole-selective rear contact. a) Sketch and HR-TEM cross-sectional images of *p*-Si solar cell with V<sub>2</sub>O<sub>x</sub>/Ag rear contact. b) Cross-sectional EDX distributions of *c*-Si/V<sub>2</sub>O<sub>x</sub>/Ag contact. c) Light *J*-*V* curves and d) EQE spectra of *p*-Si solar cells using intrinsic and HPT-V<sub>2</sub>O<sub>x</sub> rear contact. e) Simulated PCE of *p*-Si solar cells as a function of *J*<sub>0c</sub> and  $\rho_c$  at full area rear contact using Quokka 3. The marked star shows the experimental passivation and contact parameters realized by using HPT-V<sub>2</sub>O<sub>x</sub> contact. f) The PCEs of *c*-Si solar cells using TMO, such as MoO<sub>x</sub>, V<sub>2</sub>O<sub>x</sub>, WO<sub>x</sub>, and NiO<sub>x</sub>, as hole selective contacts.<sup>[19–32,46–48]</sup>

that the improved *J*<sub>sc</sub> value of the HPT-V<sub>2</sub>O<sub>x</sub> contacted solar cells is primarily attributed to the enhancement in rear surface passivation, rather than the increased transmittance of the HPT-V<sub>2</sub>O<sub>x</sub>, as demonstrated in Figure S7 (Supporting Information).

To further explore the efficiency potential of HPT-V<sub>2</sub>O<sub>x</sub>-based *p*-Si solar cells, detailed device simulations were conducted using Quokka 3, designing *p*-Si solar cells with full-area HPT-V<sub>2</sub>O<sub>x</sub> hole-selective rear contact and a line n<sup>+</sup> front contact (the same device structure as illustrated in Figure 5a). The main input parameters used in this simulation are summarized in Table S3 (Supporting Information). Based on the passivation and contact parameters achieved for the HPT-V<sub>2</sub>O<sub>x</sub> hole-selective contact (recombination current density (*J*<sub>0c</sub>) = 60 fA,  $\rho_c$  = 43 mΩ cm<sup>2</sup>), a potential PCE of over 23.2% (marked with a blue star) can be re-

alized for *p*-Si solar cells using this V<sub>2</sub>O<sub>x</sub> hole-selective rear contact, as shown in Figure 6e. According to the power and free energy loss analysis in Figure S11 (Supporting Information), the main power losses of this V<sub>2</sub>O<sub>x</sub>-based hole-selective contacted *p*-Si solar cell are primarily due to front-side emitter recombination and resistance loss, as well as rear-side contact recombination loss. Further efficiency improvements should focus on the introduction of a necessary interface passivation layer between *p*-Si and V<sub>2</sub>O<sub>x</sub> to further reduce carrier recombination at the rear side. Figure 5f summarizes recent reported *c*-Si solar cells using transition metal oxide (TMO), such as MoO<sub>x</sub>,<sup>[19–25]</sup> V<sub>2</sub>O<sub>x</sub>,<sup>[26–32]</sup> tungsten oxide (WO<sub>x</sub>),<sup>[46,47]</sup> and niobium oxide (NiO<sub>x</sub>),<sup>[48]</sup> as hole selective contacts. Compared with the limited improvement of PV performance by inserting any interfacial layers, better PV

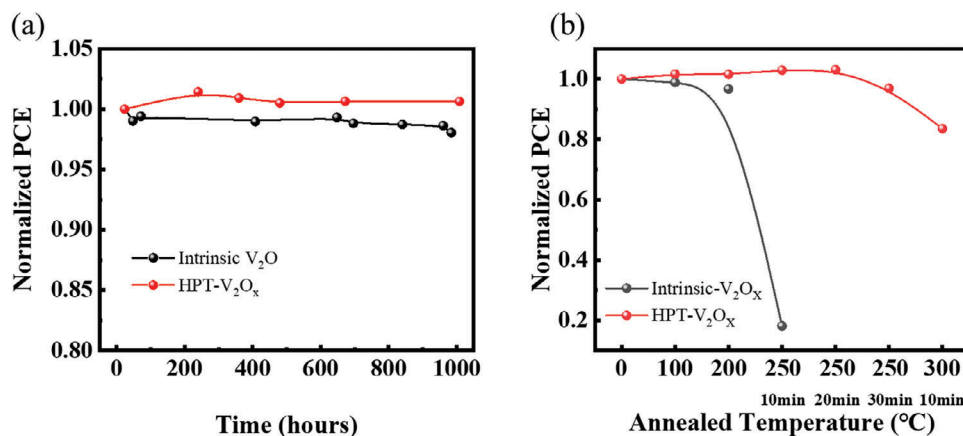


**Figure 6.** Stability of the c-Si solar cells using  $V_2O_x$  as hole selective contact. a) The long-term stability (in air, without encapsulation) and b) thermal stability of c-Si solar cells using intrinsic and HPT- $V_2O_x$  as hole selective contact.

performance is expected to be obtained by optimizing the structure and composition of the thin films, such as the HPT process.

#### 2.4. Stability of $p$ -Si/ $V_2O_x$ Solar Cells

Since TMOs are typically sensitive to humidity and temperature, it is crucial to consider the operational stability when applying these materials in c-Si solar cells. This study investigates the environmental and temperature stability of c-Si solar cells using  $V_2O_x$  as rear-side hole-selective contacts. As shown in Figure 6a and Figure S12 (Supporting Information), even without additional encapsulation, these devices demonstrate excellent environmental stability, with negligible degradation in efficiency observed over 1000 hours. To further assess the thermal stability, c-Si solar cells with  $V_2O_x$  hole-selective contacts were annealed directly in the air for 30 min at various temperatures: 100, 200, and 250 °C. The relative PV parameters as a function of annealing temperature are presented in Figure 6b and Figure S13 (Supporting Information). Compared with the intrinsic  $V_2O_x$  based device which shows terrible thermal stability at 250 °C, due to the instability of  $V_2O_x$ , the solar cell using HPT- $V_2O_x$  as hole selective contact shows a higher temperature tolerance. Even annealed at 300 °C, it can still maintain over 80% efficiency.

### 3. Conclusion

In this work, hydrogen-enriched  $V_2O_x$  films have been successfully deposited by HPT process and utilized as hole selective contact in c-Si solar cells. Compared with conventional thermal ALD process, this HPT process can induce more concentrated oxygen vacancy in the  $V_2O_x$  film, thereby improving the transport capacity of holes in the  $V_2O_x$  film, resulting in lower contact resistance loss. Further, suitable HPT process can introduce higher H concentration at the c-Si/ $V_2O_x$  interface and simultaneously reduce the C concentration, thus improving the passivation performance. The passivation and contact performance improvement have been effectively evidenced in proof-of-concept  $p$ -Si solar cells, with improved PCE close to 23% when applying this

HPT- $V_2O_x$  film as rear-side hole selective contacts. The development of this TMO deposition process with tunable photoelectric properties holds significant promise for the fabrication of efficiency, stable, and cost-effective c-Si solar cells.

### 4. Experimental Section

**Deposition of HPT- $V_2O_x$  Film:**  $V_2O_x$  films were deposited at a temperature of 200 °C by PEALD, using Vanadium (V) tri-*i*-propoxy oxide (VTIP) as the vanadium precursor and DI- $H_2O$  as the oxidant. VTIP bubbler and tube lines were heated to 40 and 120 °C, respectively. A continuous flow of argon (Ar) was used as the purge gas. One  $V_2O_x$  growth cycle consists of a VTIP pulse for 2 s, an Ar purge for 12 s, a DI- $H_2O$  pulse for 5 s, and an Ar purge for 12 s. After  $n$  (5, 10, 25, 50, 100) cycles of  $V_2O_x$ , one HPT process consisting of a pump of 20 s, an Ar/ $H_2$  (90%/10%) purge of 8 s, an Ar/ $H_2$  (90%/10%) purge plus 70W HPT of 1–10 s and an Ar purge of 12 s. (see Figure S1, Supporting Information).

**Contact and Passivation Measurement:** The contact resistivities were measured by using Transmission Line Model (TLM) method.<sup>[49]</sup> Double-side polished  $p$ -type c-Si wafers (100) with a thickness of 160  $\mu$ m and resistivity of 0.7–1.1  $\Omega$  cm were used for contact characterization. After cleaning by TMAH etching and standard Radio Corporation of America (RCA) cleaning and dilute hydrofluoric acid (HF,  $\approx$ 2% concentration) dipping, Thin  $V_2O_x$  layers (thickness calibrated by ellipsometry) were deposited by PEALD. Ag electrodes were deposited by thermal evaporation with a thickness of 300 nm through a shadow mask with TLM patterns after the  $V_2O_x$  deposition. Keithley 2400 source meter was used to measure the resistance. For the samples used for passivation measurement, the films of  $V_2O_x$  were deposited symmetrically on  $p$ -Si wafers. The effective minority carrier lifetime was characterized by photoconductance decay (Sinton WCT 120).

**Thin Films Characterization:** The composition and WF of films were characterized by XPS/UPS with a Thermo Fisher Nexsa using the Al  $K\alpha$  X-ray source ( $h\nu = 1486.6$  eV). All XPS spectra were analyzed by using casa-XPS software and deconvoluted as well as fitted using mixed Lorentzian–Gaussian line shape (GL), and all spectra were calibrated concerning carbon C 1 s peak at 284.8 eV. For the FTIR measurements, 180 and 200 cycles ( $\approx$ 10 nm) of intrinsic  $V_2O_x$  and HPT- $V_2O_x$  films were grown on one-side polished 300  $\mu$ m thick  $p$ -Si with a resistivity of 2  $\Omega$  cm. The samples were measured in a  $N_2$  atmosphere using a FTIR spectrometer (Vertex70-Hyperion3000) in transmission mode within the spectral range of 350 to 8000  $cm^{-1}$  (resolution: lower than 2  $cm^{-1}$ ). ToF-SIMS was performed by TOF-5, GmbH at sputtering energy of 1 keV. For the transmittance and absorption measurements, the optical transmittance and absorption of



$V_2O_5$  films deposition on glass substrate were examined by using UV–vis–NIR spectrophotometer (UV1920-100) with a  $BaSO_4$  integrating sphere using white glass as baseline. The contact structure was characterized by HR-TEM performed in a probe-side aberration corrected FEI Titan Tecna F20 TEM microscope operated at 200 kV.

**Solar Cell Device Fabrication:** The c-Si solar cells were fabricated on *p*-type Cz-Si wafers (resistivity of 0.7–1.1  $\Omega$  cm, thickness of 145  $\mu$ m) with the front side texturing and phosphorus doping. Front surface passivation was realized by  $SiN_x:H$  passivation and antireflection layer. The rear surface of the wafers was rinsed with diluted HF (5 wt.%) and then rinsed with deionized. Thin  $V_2O_5$  films were deposited by PEALD at a temperature of 200 °C. Subsequently, Ag (300 nm) electrodes were used as the full area rear contacts at a deposition rate of  $\approx 1$  Å  $s^{-1}$  by thermal evaporation.

**Solar Cells PV Characterization:** The PV performances of  $V_2O_5$ -based solar cells were characterized by measuring the current–voltage (*I*–*V*) characteristics with an Xe arc lamp under 100 mW  $cm^{-2}$  illumination light source (Vision vs6825, Class AAA light source), and test temperature was controlled at  $25 \pm 0.5$  °C during the measurements. A square electrode with designed opening of  $1.6 \times 1.6$   $cm^2$  was evaporated to determine the exposure area. An encapsulated standard reference c-Si solar cell certified by Fraunhofer ISE in Germany was used to calibrate the illumination intensity. The external quantum efficiencies of the solar cells were measured by Vision SR/QE testing system (Vision PVE300-IVT). The spot used for EQE measurement was focused between two fingers.

**Computational Details:** All calculations were conducted using spin-polarized DFT as implemented in the Vienna Ab initio Simulation Package (VASP 6).<sup>[50]</sup> The generalized gradient approximation (GGA) based on the Perdew–Burke–Ernzerhof (PBE) exchange–correlation functional was employed.<sup>[51,52]</sup> The projector augmented wave (PAW) method<sup>[53,54]</sup> was used to treat the core electrons and ion interactions, with the valence electrons expanded in the plane-wave basis: H 1s, Si 3s3p, O 2s2p, and V 3p3d4s. Input parameters: Grimme D3 dispersion correction was included to describe van der Waals (vdW) interactions.<sup>[55]</sup> Plane wave basis sets with cutoff energies of 450 eV for the heterojunction and 520 eV for the supercell of Si and  $V_2O_5$  were applied. The Gaussian smearing method with a smearing width of 0.05 eV was used. The convergence criteria for the self-consistent field (SCF) were set to  $10^{-6}$  eV, and the forces on each atom were set to 0.01 eV Å<sup>-1</sup> for Si and  $V_2O_5$  bulk, 0.03 eV Å<sup>-1</sup> for Si and  $V_2O_5$  surface, and 0.05 eV Å<sup>-1</sup> for the heterojunction. Geometry: The  $\alpha$ - $V_2O_5$  phase, with the orthorhombic Pmmn space group, was used as the model.<sup>[56]</sup> The bulk material parameters for  $\alpha$ - $V_2O_5$  were  $a = 3.551$  Å,  $b = 11.651$  Å,  $c = 4.338$  Å, and  $\alpha = \beta = \gamma = 90^\circ$ . For Si, the parameters were  $a = b = c = 5.469$  Å and  $\alpha = \beta = \gamma = 90^\circ$ . The Si/ $\alpha$ - $V_2O_5$  heterojunction was constructed by placing a  $2 \times 1$  relaxed four-layer  $\alpha$ - $V_2O_5$  (001) slab on a  $1 \times 2$  relaxed six-layer c-Si (111) slab. The lattice mismatches for the lattice parameters *a* and *b* were 13% and 3.2%, respectively. The bottom two layers of Si and the uppermost layer of  $V_2O_5$  atoms were fixed to represent the bulk. A vacuum zone of 15 Å was set, and both the  $\alpha$ - $V_2O_5$  (001) and Si (111) surfaces were saturated with H atoms.

## Supporting Information

Supporting Information is available from the Wiley Online Library or from the author.

## Acknowledgements

A.X. and Q.N. contributed equally to this work. This work was financially supported by the National Key R&D Program of China (2022YFB4200200), National Natural Science Foundation of China (62204266 and 62034009), Guangdong Basic and Applied Basic Research Foundation (2023A1515010767), Zhuhai Industry-University-Research Cooperation Projects (2320004002352) and Fundamental Research Funds for the Central University, Sun Yat-Sen University (23qnpy07).

## Conflict of Interest

The authors declare no conflict of interest.

## Author Contributions

J.H. conceived the idea and revised the manuscript. A.X. carried out the device fabrication, characterization, and finished the manuscript. Q.N. carried out the DFT simulation. All the authors discussed the results and provided feedback.

## Data Availability Statement

The data that support the findings of this study are available from the corresponding author upon reasonable request.

## Keywords

c-Si solar cells, hydrogen plasma treatment (HPT), passivating contact, vanadium oxide

Received: November 6, 2024  
Revised: January 30, 2025  
Published online: February 11, 2025

- [1] C. Ballif, F.-J. Haug, M. Boccard, P. J. Verlinden, G. Hahn, *Nat. Rev. Mater.* **2022**, 7, 597.
- [2] T. G. Allen, J. Bullock, X. Yang, A. Javey, S. De Wolf, *Nat. Energy* **2019**, 4, 914.
- [3] A. Richter, R. Müller, J. Benick, F. Feldmann, B. Steinhauser, C. Reichel, A. Fell, M. Bivour, M. Hermle, S. W. Glunz, *Nat. Energy* **2021**, 6, 429.
- [4] J. I. Michel, J. Dréon, M. Boccard, J. Bullock, B. Macco, *Prog. Photovolt.* **2023**, 31, 380.
- [5] J. Bullock, M. Hettick, J. Geissbühler, A. J. Ong, T. Allen, C. M. Sutter-Fella, T. Chen, H. Ota, E. W. Schaler, S. De Wolf, C. Ballif, A. Cuevas, A. Javey, *Nat. Energy* **2016**, 1, 15031.
- [6] J. Bullock, P. Zheng, Q. Jeangros, M. Tosun, M. Hettick, C. M. Sutter-Fella, Y. Wan, T. Allen, D. Yan, D. Macdonald, S. De Wolf, A. Hessler-Wyser, A. Cuevas, A. Javey, *Adv. Energy Mater.* **2016**, 6, 1600241.
- [7] L. Zhang, L. Meng, L. Cai, Z. Chen, W. Lin, N. Chen, W. Wang, H. Shen, Z. Liang, *Sol. RRL* **2021**, 5, 2100057.
- [8] K. Gao, C. Xing, D. Xu, X. Lou, X. Wang, K. Li, W. Li, J. Mao, P. Zheng, X. Zhang, X. Yang, *Small* **2024**, 20, 2310352.
- [9] C. Xing, C. Jiang, W. Gu, X. Lou, K. Gao, Y. Song, B. Shao, K. Li, X. Wang, D. Xu, X. Zhang, Y. Wang, X. Yang, B. Sun, *Prog. Photovolt.* **2024**, 32, 35.
- [10] J. Bullock, Y. Wan, M. Hettick, X. Zhaoran, S. P. Phang, D. Yan, H. Wang, W. Ji, C. Samundsett, Z. Hameiri, D. Macdonald, A. Cuevas, A. Javey, *Adv. Energy Mater.* **2019**, 9, 1803367.
- [11] X. Yang, Y. Lin, J. Liu, W. Liu, Q. Bi, X. Song, J. Kang, F. Xu, L. Xu, M. N. Hedhili, D. Baran, X. Zhang, T. D. Anthopoulos, S. DeWolf, *Adv. Mater.* **2020**, 32, 2002608.
- [12] J. He, G. Wang, Y. Qiu, Z. Tang, F. Ye, C. Zhang, S. Wang, L. Cai, T. Yu, P. Gao, *Adv. Funct. Mater.* **2022**, 32, 2205901.
- [13] W. Lin, M. Boccard, S. Zhong, V. Paratte, Q. Jeangros, L. Antognini, J. Dréon, J. Cattin, J. Thomet, Z. Liu, Z. Chen, Z. Liang, P. Gao, H. Shen, C. Ballif, *ACS Appl. Nano Mater.* **2020**, 3, 11391.
- [14] S. Zhong, J. Dreon, Q. Jeangros, E. Aydin, S. De Wolf, F. Fu, M. Boccard, C. Ballif, *Adv. Funct. Mater.* **2020**, 30, 1907840.



- [15] A. Xie, G. Wang, Y. Sun, H. Cai, X. Su, P. Cao, Z. Li, Z. Chen, J. He, P. Gao, *Prog. Photovolt.* **2024**, 32, 664.
- [16] Y. Wan, C. Samundsett, J. Bullock, M. Hettick, T. Allen, D. Yan, J. Peng, Y. Wu, J. Cui, A. Javey, A. Cuevas, *Adv. Energy Mater.* **2017**, 7, 1601863.
- [17] G. Chistiakova, B. Macco, L. Korte, *IEEE J. Photovolt.* **2020**, 10, 398.
- [18] J. Yu, M. Liao, D. Yan, Y. Wan, H. Lin, Z. Wang, P. Gao, Y. Zeng, B. Yan, J. Ye, *Nano Energy*. **2019**, 62, 181.
- [19] J. Geissbühler, J. Werner, S. Martin de Nicolas, L. Barraud, A. Hessler-Wyser, M. Despeisse, S. Nicolay, A. Tomasi, B. Niesen, S. De Wolf, C. Ballif, *Appl. Phys. Lett.* **2015**, 107, 081601.
- [20] J. Dréon, Q. Jeangros, J. Cattin, J. Haschke, L. Antognini, C. Ballif, M. Boccard, *Nano Energy*. **2020**, 70, 104495.
- [21] L. Cao, P. Procel, A. Alcañiz, J. Yan, F. Tichelaar, E. Özkol, Y. Zhao, C. Han, G. Yang, Z. Yao, M. Zeman, R. Santbergen, L. Mazzarella, O. Isabella, *Prog. Photovolt. Res. Appl.* **2022**, 31, 3638.
- [22] S. Cao, J. Li, J. Zhang, Y. Lin, L. Lu, J. Wang, M. Yin, L. Yang, X. Chen, D. Li, *Adv. Funct. Mater.* **2020**, 30, 2004367.
- [23] J. Bullock, C. Samundsett, A. Cuevas, D. Yan, Y. Wan, T. Allen, *IEEE J. Photovolt.* **2015**, 5, 1591.
- [24] L. Li, G. Du, Y. Lin, X. Zhou, Z. Gu, L. Lu, W. Liu, J. Huang, J. Wang, L. Yang, S.-T. Zhang, D. Li, *Cell Rep. Phys. Sci.* **2021**, 2, 100684.
- [25] J. Li, Q. Kang, Y. Wang, Z. Zhou, Z. Sun, H. Zhang, W. Lu, X. Tao, S.-T. Zhang, X. Chen, Z. Zheng, H. Yan, D. Li, Y. Zhang, *Adv. Funct. Mater.* **2024**, 34, 2310619.
- [26] X. Yang, H. Xu, W. Liu, Q. Bi, L. Xu, J. Kang, M. N. Hedhili, B. Sun, X. Zhang, S. De Wolf, *Adv. Electron. Mater.* **2020**, 6, 2000467.
- [27] E. R. Costals, G. Masmitjà, E. Almache, B. Pusay, K. Tiwari, E. Saucedo, C. J. Raj, B. C. Kim, J. Puigdollers, I. Martín, C. Voz, P. Ortega, *Mater. Adv.* **2022**, 3, 337.
- [28] G. Masmitjà, L. G. Gerling, P. Ortega, J. Puigdollers, I. Martín, C. Voz, R. Alcubilla, *J. Mater. Chem. A*. **2017**, 5, 9182.
- [29] Z. Liu, W. Lin, Z. Chen, D. Chen, Y. Chen, H. Shen, Z. Liang, *Adv. Mater. Interfaces*. **2022**, 9, 2102374.
- [30] G. Du, L. Li, X. Yang, X. Zhou, Z. Su, P. Cheng, Y. Lin, L. Lu, J. Wang, L. Yang, X. Gao, X. Chen, D. Li, *Adv. Mater. Interfaces*. **2021**, 8, 2100989.
- [31] G. Du, L. Li, H. Zhu, L. Lu, X. Zhou, Z. Gu, S.-T. Zhang, X. Yang, J. Wang, L. Yang, X. Chen, D. Li, *EcoMat*. **2022**, 4, 12175.
- [32] D. Xu, Q. Bi, K. Li, K. Gao, X. Wang, W. Shi, S. Wang, C. Xing, X. Zhang, X. Yang, *Adv. Funct. Mater.* **2024**, 34, 2407290.
- [33] H. Wei, L. Meng, Z. Liu, W. Wang, N. Chen, Y. Hong, Y. Chen, H. Shen, Z. Liang, *Small*. **2023**, 19, 2300879.
- [34] H. Cheng, Z. Huang, L. Zhang, Y. Liu, X. Song, R. Tong, S. Zhong, L. Shi, X. Kong, W. Shen, *Sol. Energy*. **2022**, 247, 171.
- [35] L. Li, L. Ying, Y. Lin, X. Li, X. Zhou, G. Du, Y. Gao, W. Liu, L. Lu, J. Wang, L. Yang, S.-T. Zhang, D. Li, *Adv. Funct. Mater.* **2022**, 32, 2207158.
- [36] O. Almora, L. G. Gerling, C. Voz, R. Alcubilla, J. Puigdollers, G. Garcia-Belmonte, *Sol. Energy Mater. Sol. Cells*. **2017**, 168, 221.
- [37] L. G. Gerling, S. Mahato, A. Morales-Vilches, G. Masmitjà, P. Ortega, C. Voz, R. Alcubilla, J. Puigdollers, *Sol. Energy Mater. Sol. Cells*. **2016**, 145, 109.
- [38] W. Wang, J. He, L. Cai, Z. Wang, S. K. Karuturi, P. Gao, W. Shen, *Sol. RRL* **2020**, 4, 2000569.
- [39] T. G. Allen, J. Bullock, P. Zheng, B. Vaughan, M. Barr, Y. Wan, C. Samundsett, D. Walter, A. Javey, A. Cuevas, *Prog. Photovolt.* **2017**, 25, 636.
- [40] D. Barreca, L. Armelao, F. Caccavale, V. Di Noto, A. Gregori, G. A. Rizzi, E. Tondello, *Chem. Mater.* **2000**, 12, 98.
- [41] J. Musschoot, D. Deduytsche, H. Poelman, J. Haemers, R. L. Van Meirhaeghe, S. Van den Berghe, C. Detavernier, *J. Electrochem. Soc.* **2009**, 156, P122.
- [42] K. Van de Kerckhove, F. Mattelaer, J. Dendooven, C. Detavernier, *Dalton Trans.* **2017**, 46, 4542.
- [43] W. Liu, L. Zhang, X. Yang, J. Shi, L. Yan, L. Xu, Z. Wu, R. Chen, J. Peng, J. Kang, K. Wang, F. Meng, S. De Wolf, Z. Liu, *Joule*. **2020**, 4, 913.
- [44] A. Ali, T. Gouveas, M.-A. Hasan, S. H. Zaidi, M. Asghar, *Sol. Energy Mater. Sol. Cells*. **2011**, 95, 2805.
- [45] M. Choi, A. Janotti, C. G. Van de Walle, *ACS Appl. Mater. Interfaces*. **2014**, 6, 4149.
- [46] M. Mews, L. Korte, B. Rech, *Sol. Energy Mater. Sol. Cells*. **2016**, 158, 77.
- [47] L. G. Gerling, S. Mahato, C. Voz, R. Alcubilla, J. Puigdollers, *Appl. Sci.* **2015**, 5, 695.
- [48] W. Zhang, H. Shen, M. Yin, L. Lu, B. Xu, D. Li, *ACS Omega*. **2022**, 7, 16494.
- [49] G. K. Reeves, H. B. Harrison, *IEEE Electron Device Lett.* **1982**, 3, 111.
- [50] J. Hafner, *J. Comput. Chem.* **2008**, 29, 2044.
- [51] G. Kresse, J. Hafner, *Phys. Rev. B*. **1993**, 48, 13115.
- [52] J. P. Perdew, K. Burke, M. Ernzerhof, *Phys. Rev. Lett.* **1996**, 77, 3865.
- [53] P. E. Blöchl, *Phys. Rev. B*. **1994**, 50, 17953.
- [54] G. Kresse, D. Joubert, *Phys. Rev. B*. **1999**, 59, 1758.
- [55] S. Grimme, J. Antony, S. Ehrlich, H. Krieg, *J. Chem. Phys.* **2010**, 132, 154104.
- [56] C. Delmas, H. Cognac-Auradou, J. M. Cocciantelli, M. Ménétrier, J. P. Doumerc, *Solid State Ionics*. **1994**, 69, 257.